Design of Flame-Made ZnZrOx Catalysts for Sustainable Methanol Synthesis from CO2

Journal Article

Author(s):
Pinheiro Araújo, Thaylan; Morales-Vidal, Jordi; Zou, Tangsheng; Agrachev, Mikhail; Verstraeten, Simon; Willi, Patrik O.; Grass, Robert N.; Jeschke, Gunnar; Mitchell, Sharon; López, Núria; Pérez-Ramírez, Javier

Design of Flame-Made ZnZrO$_x$ Catalysts for Sustainable Methanol Synthesis from CO$_2$

Thaylan Pinheiro Araújo, Jordi Morales-Vidal, Tangsheng Zou, Mikhail Agrachev, Simon Verstraeten, Patrik O. Willi, Robert N. Grass, Gunnar Jeschke, Sharon Mitchell, Núria López, and Javier Pérez-Ramírez*

Mixed zinc-zirconium oxides, ZnZrO$_x$, are highly selective and stable catalysts for CO$_2$ hydrogenation to methanol, a pivotal energy vector. However, their activity remains moderate, and descriptors to design improved systems are lacking. This work applies flame spray pyrolysis (FSP), a one-step and scalable method, to synthesize a series of ZnZrO$_x$ catalysts, and systematically compares them to coprecipitated (CP) analogs to establish deeper synthesis–structure–performance relationships. FSP systems (up to 5 mol%) generally display a threefold higher methanol productivity compared to their CP counterparts. In-depth characterization and theoretical simulations show that, unlike CP, FSP maximizes the surface area and formation of atomically dispersed Zn^{2+} sites incorporated in lattice positions within the ZrO$_2$ surface, which is key to improving performance. Analysis by in situ electron paramagnetic resonance (EPR) spectroscopy reveals that the specific architecture of the flame-made catalyst markedly fosters the generation of oxygen vacancies. Together with surrounding Zn and Zr-O atoms, the oxygen vacancies create active ensembles that favor methanol formation through the formate path while suppressing undesired CO production, as confirmed by kinetic modeling. This study elucidates the nature of active sites and their working mechanism, pushing forward ZnZrO$_x$-catalyzed methanol synthesis by providing a new benchmark for this cost-effective and earth-abundant catalyst family.

1. Introduction

Methanol (CH$_3$OH) is a versatile energy carrier, with an annual capacity of over 4 million metric ton and demand fore-casted to exceed production capacities by 2023.[1,2] It can be used as a fuel additive or directly applied to power fuel cells and, as is done nowadays, combustion engines used in the maritime shipping industry.[1–3] However, methanol production presently relies on fossil feedstocks and therefore needs to urgently align with global efforts tackling climate change by lowering carbon footprint.[1,2,4,5] In this context, thermocatalytic conversion of captured carbon dioxide (CO$_2$) and renewable hydrogen (H$_2$) into methanol (CO$_2$ + 3H$_2$ ⇌ CH$_3$OH + H$_2$O) is a strategic route to enable its sustainable production and, consequently, defossilization of various chemical and energy value chains.[1,2,5,6] In the past decade, major efforts have been devoted to identify promising catalytic materials, which can be broadly divided into copper (Cu), palladium (Pd), indium oxide (In$_2$O$_3$), and zinc-zirconia (ZnZrO$_x$) based families.[2,5,7–9] Among them, mixed reducible oxides, such as ZnZrO$_x$, represent cost effective and earth abundant competitive choices.[10–13] In particular, these systems display a high methanol selectivity by limiting the undesired carbon monoxide (CO) formation through the reverse water-gas shift (RWGS) reaction (CO$_2$ + H$_2$ ⇌ CO + H$_2$O).[10–12] Moreover, ZnZrO$_x$ catalysts show excellent stability for several

T. Pinheiro Araújo, T. Zou, S. Verstraeten, P. O. Willi, R. N. Grass, S. Mitchell, J. Pérez-Ramírez
Institute of Chemical and Bioengineering
Department of Chemistry and Applied Biosciences
ETH Zurich
Vladimir-Prelog-Weg 1, Zurich 8093, Switzerland
E-mail: jpr@chem.ethz.ch

The ORCID identification number(s) for the author(s) of this article can be found under https://doi.org/10.1002/aenm.202204122.

J. Morales-Vidal, N. López
Institute of Chemical Research of Catalonia (ICIQ)
The Barcelona Institute of Science and Technology
Av. Països Catalans 16, Tarragona 43007, Spain

J. Morales-Vidal
Universitat Rovira i Virgili
Av. Catalunya 35, Tarragona 43002, Spain

M. Agrachev, G. Jeschke
Laboratory of Physical Chemistry
Department of Chemistry and Applied Biosciences
ETH Zurich
Vladimir-Prelog-Weg 2, Zurich 8093, Switzerland

**ADVANCED
SCIENCE NEWS**

www.advancedsciencenews.com

**ADVANCED
ENERGY
MATERIALS**

www.advenergymat.de

hundred hours on stream and high resistance to poisoning by impurities present in CO_2-containing streams, such as hydrogen sulfide, sulfur dioxide, and CO.[10,14]

In general, $ZnZrO_x$ catalysts are prepared by coprecipitation (CP) instead of impregnation methods as forming a solid solution phase was considered key to obtaining high space-time yields of methanol.[10,12,13,15] Specifically, CO_2 and H_2 activation to produce methanol reportedly proceeds via a bifunctional mechanism involving both Zn^{2+} and Zr^{4+} cations acting as active sites. Hence, introducing single zinc sites into the lattice of ZrO_2 was considered a vital step.[10,12,13] However, these catalytic systems still require productivity improvements to reach effective industrial implementation, which is hindered by several factors. Firstly, CP tends to induce zinc incorporation not only into lattice positions within the ZrO_2 surface but especially into its bulk phase, which leads to detrimental effects such as materials with relatively low specific surface area (i.e., 30–40 m^2 g_{cat}^{-1}).[10,12,15] Besides, zinc fosters the formation of tetragonal ZrO_2 (t-ZrO_2), which possesses inferior CO_2 adsorption capacity compared to monoclinic ZrO_2 (m-ZrO_2).[10,11,16,17] More importantly, while a deep understanding of descriptors governing reactivity and stability is paramount to guide catalyst design, such crucial aspects are still poorly understood for $ZnZrO_x$. To our knowledge, no study has addressed the impact of catalyst architecture (i.e., zirconia polymorph and zinc location and speciation) on the performance thoroughly. Furthermore, it is well established that surface oxygen vacancies act as active sites for other relevant reducible oxides (i.e., In_2O_3[18–20]). Still, their role in forming catalytic ensembles, and their structure and working mechanism remain elusive for $ZnZrO_x$. Based on these observations, it is clear that the rational design of superior $ZnZrO_x$ catalysts requires alternative synthesis methods and detailed investigations devised to uncover synthesis–structure–performance relationships.

In this contribution, we applied flame spray pyrolysis (FSP) to prepare and systematically investigate a platform of $ZnZrO_x$ catalysts with a broad range of compositions (i.e., 0–100 mol% Zn), which exhibit superior performance compared to state-of-the-art CP materials. FSP was selected as a one-step and scalable synthesis method that offers effective control over the nanostructure of the synthesized materials.[20–23] Specially, FSP favors the surface deposition of active metal species on carriers without promoting bulk incorporation, a classic drawback of CP methods.[20,23,24] Indeed, the flame-made $ZnZrO_x$ catalysts exhibit enhanced surface area and preferential formation of atomically dispersed Zn^{2+} sites incorporated in lattice positions at the ZrO_2 surface, as revealed by extensive in-depth characterization and density functional theory (DFT) simulations. Combined in situ electron paramagnetic resonance (EPR) spectroscopy, DFT, and kinetic modeling investigations offer insights into the relationship between the catalyst architecture and oxygen vacancy formation, the resulting structure of active ensembles, and reactivity patterns in CO_2 hydrogenation to methanol. Our study provides an atomic-level rationalization of active sites, their correlation to experimental fingerprints and their working mechanism, and reveals a new benchmark for $ZnZrO_x$-catalyzed methanol synthesis.
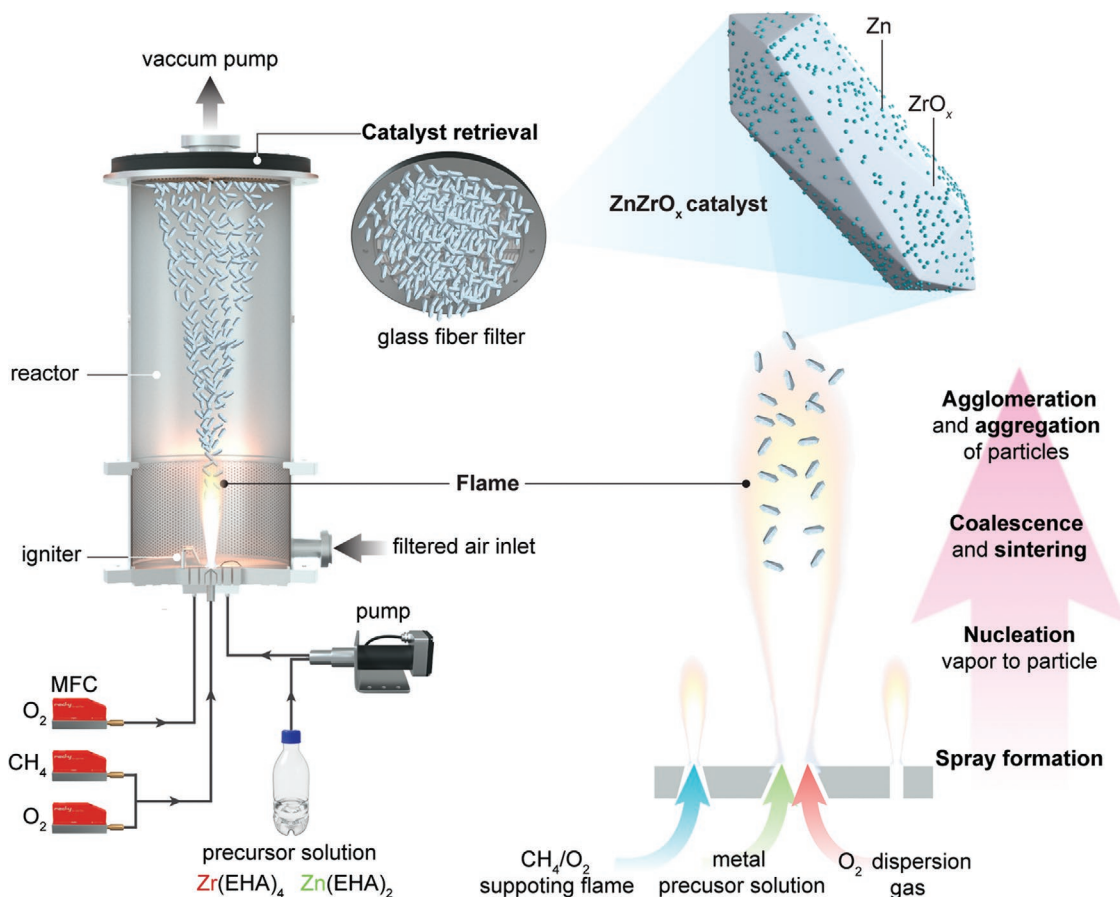
2. Results and Discussion

2.1. Optimal Catalyst Synthesis Route and Zinc Content

Mixed zinc-zirconia catalysts of varying composition were prepared by FSP (**Figure 1**, 0.75–95 mol% Zn, coded as $\gamma ZnZrO_x$, γ = 0.75–95) and CP (1.5–28 mol% Zn, coded as $\gamma ZnZrO_x$,CP, γ = 1.5–28). X-ray fluorescence spectroscopy (XRF) confirmed that the zinc content matched closely the nominal value for all materials (Table S1, Supporting Information). Evaluation in CO_2 hydrogenation to methanol at typical reaction conditions (593 K and 5 MPa) showed that FSP catalysts considerably outperform their coprecipitated counterparts in terms of methanol space-time yield (STY, **Figure 2**a and Table S2, Supporting Information). In general, methanol productivity over CP catalysts follows a typical volcano trend, reaching maximum performance at 13 mol% of zinc (STY = 0.27 g_{MeOH} h^{-1} g_{cat}^{-1}), with higher content (i.e., 28 mol%) leading to ≈35% drop in methanol STY (Figure 2a), which is likely caused by phase segregation, in line with a previous report.[10] In contrast, methanol STY over FSP systems starkly increases with zinc content up to 5 mol% (STY = 0.46 g_{MeOH} h^{-1} g_{cat}^{-1}), slightly decreases for the 13 and $28ZnZrO_x$ samples (STY = 0.39–0.42 g_{MeOH} h^{-1} g_{cat}^{-1}), and then significantly diminishes upon addition of higher contents (STY = 0.29 g_{MeOH} h^{-1} g_{cat}^{-1}), due to ZnO becoming the main phase, which is less active (Figure 2a). Interestingly, the $5ZnZrO_x$ catalyst prepared by FSP displays an approximately twofold higher methanol STY compared to the most active CP system ($13ZnZrO_x$,CP) with a ≈60% lower zinc content. This suggests that the inferior performance of CP catalysts is likely due to the synthesis approach, triggering incorporation of a substantial portion of zinc within the bulk of zirconia. Assessing methanol selectivity (S_{MeOH}) at similar CO_2 conversion (X_{CO2}) levels indicates that the trend in methanol STY with respect to zinc content observed for FSP and CP catalysts is directly linked to that of S_{MeOH} (Figure 2b). In fact, S_{MeOH} remains virtually unchanged over FSP systems containing 5–28 mol% of zinc (≈80%), whereas it clearly reaches its maximum for $13ZnZrO_x$,CP (≈80%) and drops to 50% for $28ZnZrO_x$,CP. This hints that FSP offers a better control than CP at maximizing active sites that limit CO formation through the RWGS. Additionally, when compared at the same X_{CO2} (7%), CP and FSP samples featuring 13 mol% of zinc show similar S_{MeOH} (≈80%, Figure 2b), suggesting that their active sites for methanol formation likely possess similar structure. Hence, their performance difference originates from FSP systems being more active in comparison to CP catalysts (Table S2, Supporting Information).

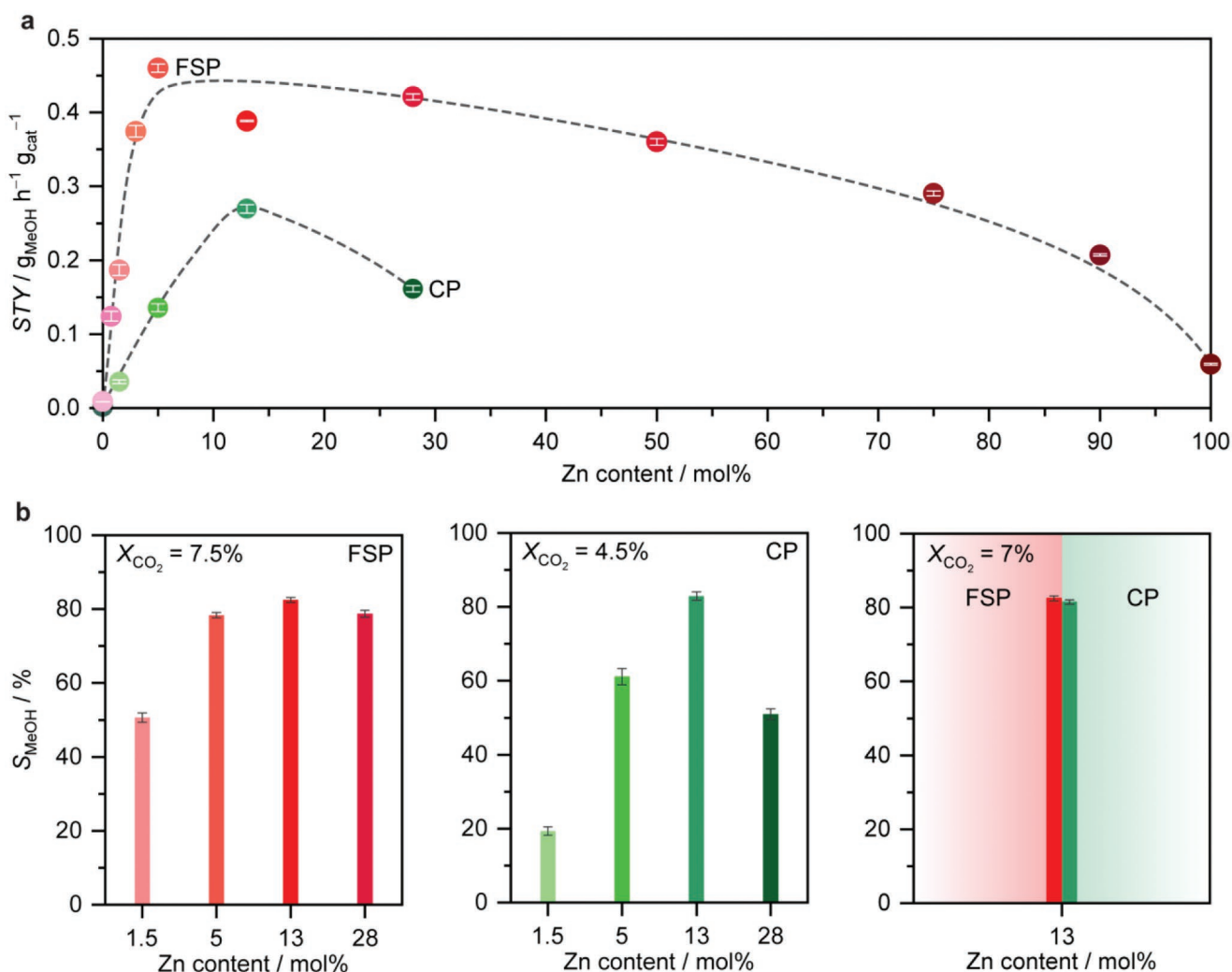### 2.2. Characterization of Zinc Speciation and Zirconia Structure

In-depth characterization was carried out to rationalize the behavior of FSP and CP systems. Determination of the crystal structure and phase composition of the catalysts by X-ray diffraction (XRD, **Figure 3**a, Figures S1 and S2 and Tables S3 and S4, Supporting Information) showed that fresh FSP catalysts (up to 28 mol% Zn) contain a mixture of monoclinic (20–40%)

**ADVANCED
SCIENCE NEWS**
www.advancedsciencenews.com

**ADVANCED
ENERGY
MATERIALS**
www.advenergymat.de

Figure 1. Scheme of the flame spray pyrolysis (FSP) setup and method used for the preparation of ZnZrO$_x$ catalysts.

and tetragonal or cubic (60–80%) zirconia (m-, t-, and c-ZrO$_2$, respectively), as t and c phases cannot be distinguished by XRD (Figure 3a and Figure S1 and Table S3, Supporting Information). The m- and t- or c-ZrO$_2$ relative compositions show no correlation with the zinc content whereas zinc oxide (ZnO) is detected and becomes the predominant phase upon addition of 13 and 75 mol% of zinc, respectively (Figure 3a and Figure S1 and Table S3, Supporting Information). At lower contents, zinc is most likely embedded into the ZrO$_2$ lattice, forming a solid solution, or supported as ZnO clusters or nanoparticles smaller than ≈4 nm, the detection limit of the XRD instrument. In contrast, CP catalysts in fresh form generally crystalize into a pure t-ZrO$_2$ phase, with m-ZrO$_2$ (17%) and ZnO (20%) phases being detected only for the 1.5 and 28ZnZrO$_x$,CP samples, respectively (Figure S2 and Table S4, Supporting Information), which is in line with previous reports.[10,12] The presence of m-ZrO$_2$ is likely due to the low zinc content in the 1.5ZnZrO$_x$,CP sample, which is insufficient to stabilize the t-ZrO$_2$ polymorph, whereas ZnO is formed because the amount of zinc could still be higher than the saturation point of the ZnZrO$_x$ solid solution; triggering phase segregation.[10] Upon reaction, the amount of m-ZrO$_2$ and ZnO slightly increased while that of t-ZrO$_2$ decreased for all FSP systems containing up to 28 mol% of zinc (Figure 3a and Figure S1 and Table S3, Supporting Information), hinting at some degree of catalyst restructuring. In the case of CP materials in used form (catalysts recovered after 12 h on stream), no detectable

change in the ZrO$_2$ phase composition was observed, except for the 1.5ZnZrO$_x$,CP sample in which the content of m-ZrO$_2$ increased to 25%, likely due to t–m transformation triggered by water formed under reaction (Figure S3 and Table S4, Supporting Information).[25] The crystallite size of m- and t-ZrO$_2$ was also estimated for fresh and used catalysts using the Scherrer equation (Tables S2 and S4, Supporting Information), but no correlation with the synthesis method, Zn content, or catalytic performance is observed. Consistent with the expected incorporation of zinc into lattice positions of the ZrO$_2$ bulk phase, the main reflection characteristic of t-ZrO$_2$ (≈30° 2θ) shifts to higher angles with increasing Zn content (Figure S3a, Supporting Information), indicating that zinc is incorporated at lattice positions within the ZrO$_2$ bulk phase, confirming the formation of a solid solution.[10] Remarkably, this phenomenon is not observed for FSP catalysts (Figure S3b, Supporting Information), suggesting that this method does not lead to bulk incorporation of zinc atoms, but rather disperse them at surface lattice positions of the ZrO$_2$ carrier, with the metal surplus likely agglomerating into ZnO clusters and/or nanoparticles. X-ray photoelectron spectroscopy (XPS, Table S5, Supporting Information) revealed closely matched zinc surface and bulk compositions for 5ZnZrO$_x$, which remain unaltered upon reaction, indicating that zinc is indeed highly dispersed and located at the surface rather than the bulk sites of ZrO$_2$. Similarly, the presence of ZnO detected by XRD for 13 and 28ZnZrO$_x$ is accompanied by a

2204122 (3 of 17)

**ADVANCED
SCIENCE NEWS**

www.advancedsciencenews.com

**ADVANCED
ENERGY
MATERIALS**

www.advenergymat.de

Figure 2. a) Methanol space-time yield (STY) and b) selectivity (S_{MeOH}) during CO_2 hydrogenation over $ZnZrO_x$ catalysts prepared by flame spray pyrolysis (FSP) and coprecipitation (CP). Averaged values measured over 12 h on stream are presented with their corresponding error bars. Reaction conditions: T = 593 K, P = 5 MPa, H_2/CO_2 = 4, and GHSV = 24 000 cm^3 h^{-1} g_{cat}^{-1}.

decrease in the Zn surface concentration (Table S5, Supporting Information), which is expected as sintering diminishes the amount of Zn atoms exposed at the catalyst surface. Finally, the amount of Zn at the surface of all fresh and used CP materials is significantly lower compared to its total content (Table S5, Supporting Information), which further confirms that a substantial portion of zinc is incorporated into ZrO_2 bulk phase during CP (Figure S3a, Supporting Information). A detailed discussion on zinc surface composition of FSP and CP catalysts can be found in Section S1.1 (Supporting Information).

To gain additional insights into the surface structure of the catalysts, fresh and used samples were analyzed by UV Raman spectroscopy using a 325 nm laser (Figure 3b). In principle, by varying the laser source, one can identify which oxide phase is present at different particle depths, from bulk to skin layers (≈10 nm).[26,27] Interestingly, two distinct trends emerge for FSP catalysts. The surface of fresh samples with low Zn content (i.e., 1.5 and 5 mol%) mainly comprise of t-ZrO_2 (bands located at 145, 265, 315, 460, and 642 cm^{-1}),[28–30] which almost

fully transformed into a monoclinic phase (bands located at 180, 305, 378, 473, and 625 cm^{-1})[28] upon CO_2 hydrogenation. In contrast, higher zinc contents (i.e., 13 and 28 mol%) lead to catalysts with enriched cubic surface structure (bands located at 564 cm^{-1})[10] in fresh form, which remains virtually unaltered upon reaction, except for some m-ZrO_2 being also formed. Unfortunately, CP catalysts revealed themselves fluorescent when exposed to the 325 nm laser, which prevented the acquisition of Raman spectra. Such behavior has been reported for ZrO_2,[28,31,32] and more generally for other metal oxides, and attributed to the defect generation in the lattice.[27] This observation corroborates XRD and XPS findings showing that CP catalysts experience incorporation of zinc to the bulk of ZrO_2, which likely creates additional structural defects.

Investigations by microscopy coupled to energy-dispersive X-ray (EDX) spectroscopy revealed that FSP promotes atomic dispersion of zinc on ZrO_2 for contents up to 5 mol%, while the formation of ZnO nanoparticles occurs with higher amounts of zinc (**Figure 4**a). This "switch" in zinc speciation
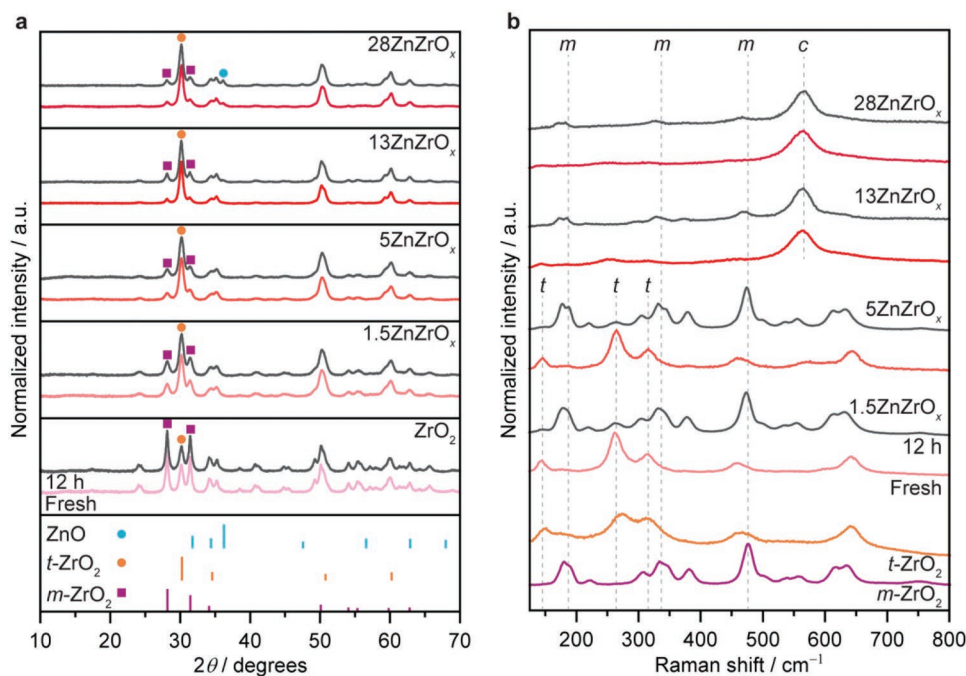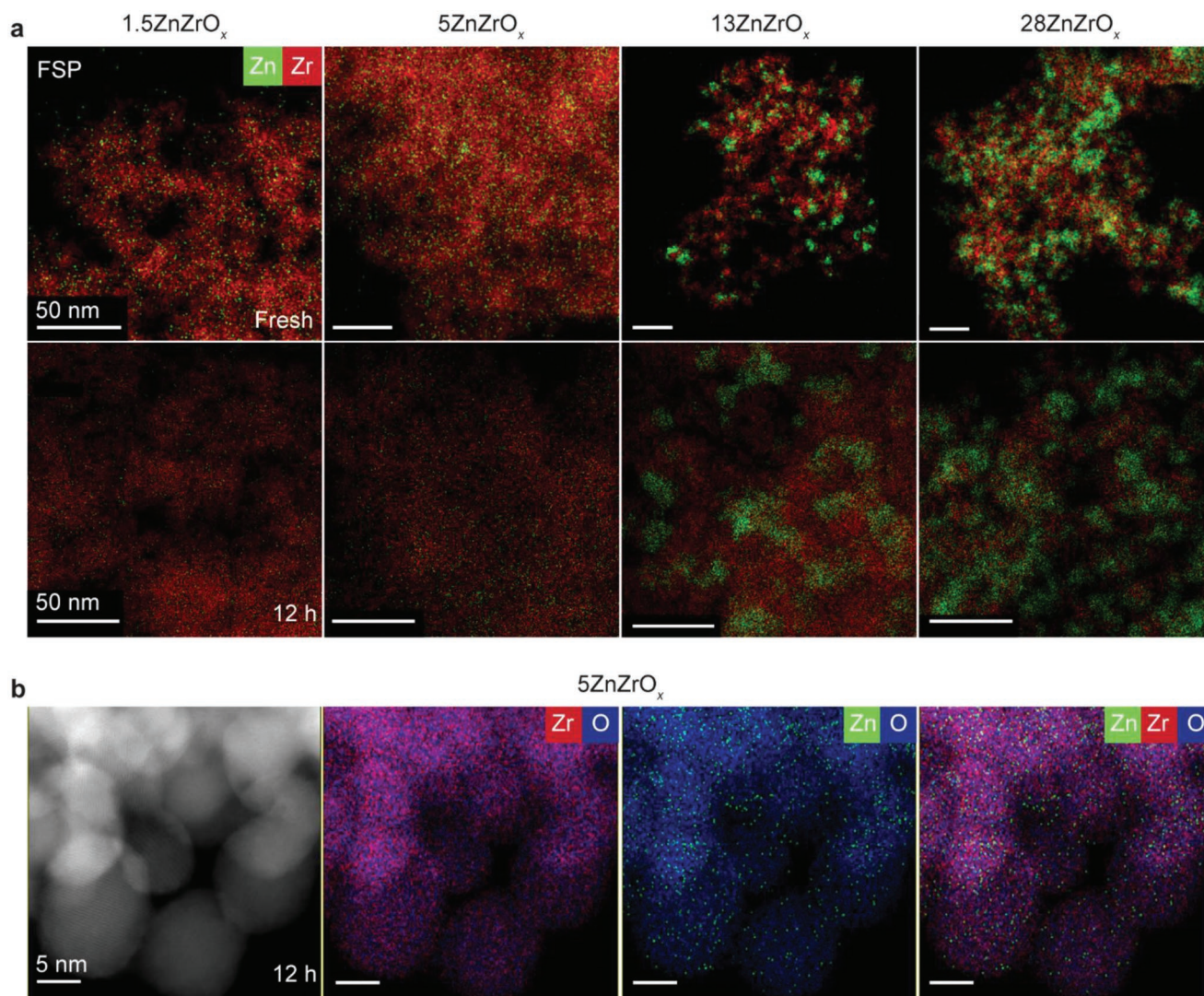
Figure 3. a) X-ray diffraction (XRD) patterns and b) Raman spectra of flame spray pyrolysis (FSP) made ZnZrO$_x$ catalysts in fresh form and after CO$_2$ hydrogenation for 12 h with t- and m-ZrO$_2$ carriers serving as reference. Reference patterns of pure phases are shown with vertical lines in the bottom panel. Reaction conditions: T = 593 K, P = 5 MPa, H$_2$/CO$_2$ = 4, and GHSV = 24 000 cm^3 h^{-1} g$_{cat}^{-1}$.

for FSP systems coincides with the plateau in methanol STY experienced by 13 and 28ZnZrO$_x$ (Figure 2a) and suggests that atomically dispersed species likely saturate the surface sites at 5 mol% and excess zinc present in ZnO nanoparticles formed at higher contents likely spectate in the reaction. The zinc speciation remains unaltered over FSP catalysts upon reaction, particularly for the 5ZnZrO$_x$ sample (Figure 4a,b). In contrast, while zinc is also atomically dispersed in freshly coprecipitated materials even at high contents (i.e., 13 mol%, Figure S4, Supporting Information), most used samples (1.5 and 5ZnZrO$_{x,}$CP) show some degree of sintering. Still, the 13ZnZrO$_{x,}$CP is markedly stable with no sign of zinc agglomeration whereas severe phase segregation is present in both fresh and used 28ZnZrO$_{x,}$CP (Figure S4, Supporting Information). This observation most likely explains the volcano-shaped trend of CP catalysts (Figure 2), as ZnO is much less active in CO$_2$ hydrogenation to methanol[10] and can potentially cover and block some active sites of ZnZrO$_x$. Finally, characterization of 5ZnZrO$_x$ 13ZnZrO$_{x,}$CP catalysts by high resolution transmission microscopy (HRTEM, Figure S5, Supporting Information) confirmed the high crystalline order in both samples. Consistent with the high dispersion of Zn, the observed lattice fringes correspond to ZrO$_2$. In agreement with XRD findings, the fresh and used 5ZnZrO$_x$ samples exhibit d-spacings characteristic of the tetragonal and monoclinic phases, while only the former are present in 13ZnZrO$_{x,}$CP.

Quasi in situ X-ray absorption near-edge structure spectra at the Zn K-edge (XANES, **Figure 5**a) of used FSP 5 and 13ZnZrO$_x$, directly isolated from the reactor without exposure to air, indicate the presence of Zn^{2+} in both catalysts, especially when compared to those of hexagonal ZnO (h-ZnO) and Zn metal foil references (Figure 5a). Still, some features present

in the XANES spectrum of h-ZnO are substantially dampened in the lower-content catalyst, hinting at higher disorder in the Zn local structure, which could be explained by its atomic dispersion and thus stronger interaction with the ZrO$_2$ lattice, in line with previous reports.[33,34] For 13ZnZrO$_x$, its XANES spectrum closely resemble that of h-ZnO, which agrees with microscopy findings evidencing the formation of ZnO nanoparticles (Figure 4a). Analysis of the extended X-ray absorption fine structure (EXAFS), Figure 5b and Table S6, Supporting Information) shows that both Zn–O and Zn–Zn scattering paths are present in the 13ZnZrO$_x$ catalyst whereas only the Zn–O feature with the total number of first oxygen neighbors of ≈2 was observed for 5ZnZrO$_x$.[33,34] This confirms that the latter comprises of highly dispersed and isolated zinc atoms located within the surface lattice of ZrO$_2$, while ZnO particles additionally exist in higher-content samples. XPS (Figure S6a,b, Supporting Information) further supported that surface zinc species are oxidized in all fresh and used FSP samples, as suggested by the absence of signals characteristic of metallic zinc in the Zn LMM Auger spectra.

Considering that FSP generally produces materials with improved textural properties,[35] the specific surface area (S_{BET}) of both CP and FSP samples was determined by N$_2$ sorption (**Figure 6**a and Tables S3 and S4, Supporting Information). Remarkably, FSP materials display a twofold higher S_{BET} in comparison to their CP counterparts, which is consistent with their superior catalytic performance. More specifically, the S_{BET} of freshly coprecipitated systems drastically diminishes (from ≈70 to 20 m^2 g^{-1}) with increasing zinc content (from 0 to 28 mol%), hinting at zinc behaving as a detrimental structure modifier, likely due to its incorporation into the bulk phase of ZrO$_2$. In contrast, the S_{BET} of FSP catalysts in fresh form

ADVANCED
SCIENCE NEWS
www.advancedsciencenews.com

ADVANCED
ENERGY
**MATERIALS**
www.advenergymat.de

Figure 4. a) Energy-dispersive X-ray (EDX) maps of flame spray pyrolysis (FSP) made $ZnZrO_x$ catalysts in fresh form and after CO_2 hydrogenation for 12 h. b) High magnification scanning transmission electron microscopy high-angle annular dark-field (STEM-HAADF) image and corresponding EDX maps of the FSP-made $5ZnZrO_x$ catalyst after CO_2 hydrogenation for 12 h. Reaction conditions: $T = 593$ K, $P = 5$ MPa, $H_2/CO_2 = 4$, and GHSV = 24 000 cm^3 h^{-1} g_{cat}^{-1}.

increases (from 65 to 90 m^2 g^{-1}) with the amount of zinc (up to 5 mol%), but decreases (≈65–30 m^2 g^{-1}) for higher-content samples (i.e., 13–100 mol% Zn) owing to the formation of ZnO nanoparticles. No significant variation in the S_{BET} was detected for used CP and FSP catalysts (Tables S3 and S4, Supporting Information), which is line with their stable methanol productivity. Besides, methanol STY values normalized by S_{BET} (see inset Figure 6a) further highlight that the enhanced surface area of FSP in comparison with CP samples noticeably contributes to their improved performance at low zinc content (up to 5 mol%), where the zinc speciation is homogenous. Interestingly, volumetric CO_2 chemisorption measured at reaction temperature (593 K, Figure 6b) revealed that methanol STY linearly correlates with the CO_2 uptake of FSP catalysts containing up to 5 mol% of Zn. This provides additional evidence that highly dispersed and isolated zinc sites present at the catalyst surface, particularly for $5ZnZrO_x$, are paramount to form the catalytic

ensemble and suggest that maximizing such speciation is crucial to ensure maximal methanol productivity.

With sound experimental analyses indicating that the most active FSP and CP systems possess analogous catalytic ensembles, their structure was further examined by DFT. Since all three ZrO_2 polymorphs (*m*-ZrO_2, *t*-ZrO_2, and *c*-ZrO_2) were detected for $ZnZrO_x$ catalysts, their relative stability in undoped and Zn-doped forms was investigated. The computed formation energy (E_f, Equations S1 and S2, Supporting Information) shows that monoclinic is the most stable polymorph of zinc-free ZrO_2, followed by *t*-, and *c*- which are 0.11 and 0.21 eV per formula unit less stable, respectively. Considering that zinc incorporation was shown to occur at distinct sites of ZrO_2 depending on the preparation method, and that the stability of the resulting ZrO_2 polymorph is governed by the interplay between the zinc structure and location, as well as the creation of oxygen vacancies, the potential effects were assessed for both bulk and surfaces of
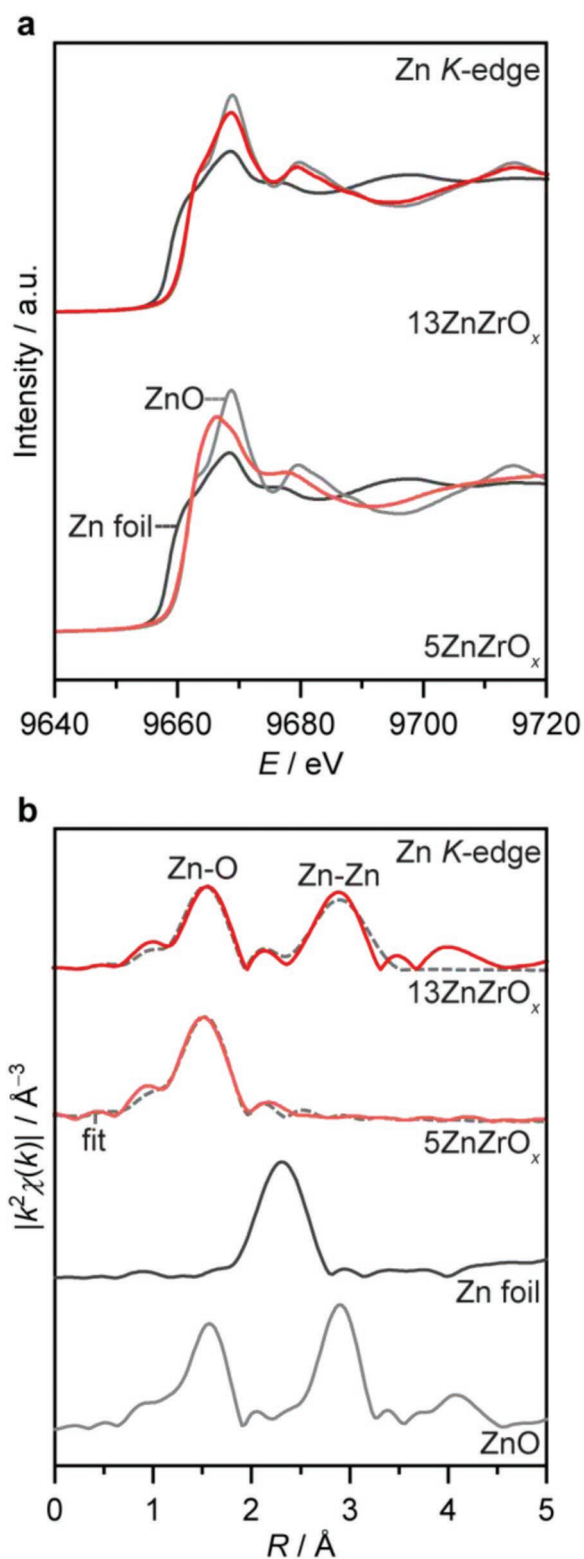
Figure 5. a) k-weighted Zn K-edge X-ray absorption near-edge structure (XANES), and b) extended X-ray absorption fine structure (EXAFS) spectra of flame spray pyrolysis (FSP) made ZnZrO$_x$ systems, with fit model and spectra of ZnO and metallic Zn serving as references, for catalysts after CO$_2$ hydrogenation for 20 h. Reaction conditions: T = 593 K, P = 5 MPa, H$_2$/CO$_2$ = 4, and GHSV = 24 000 cm^3 h^{-1} g$_{cat}^{-1}$.
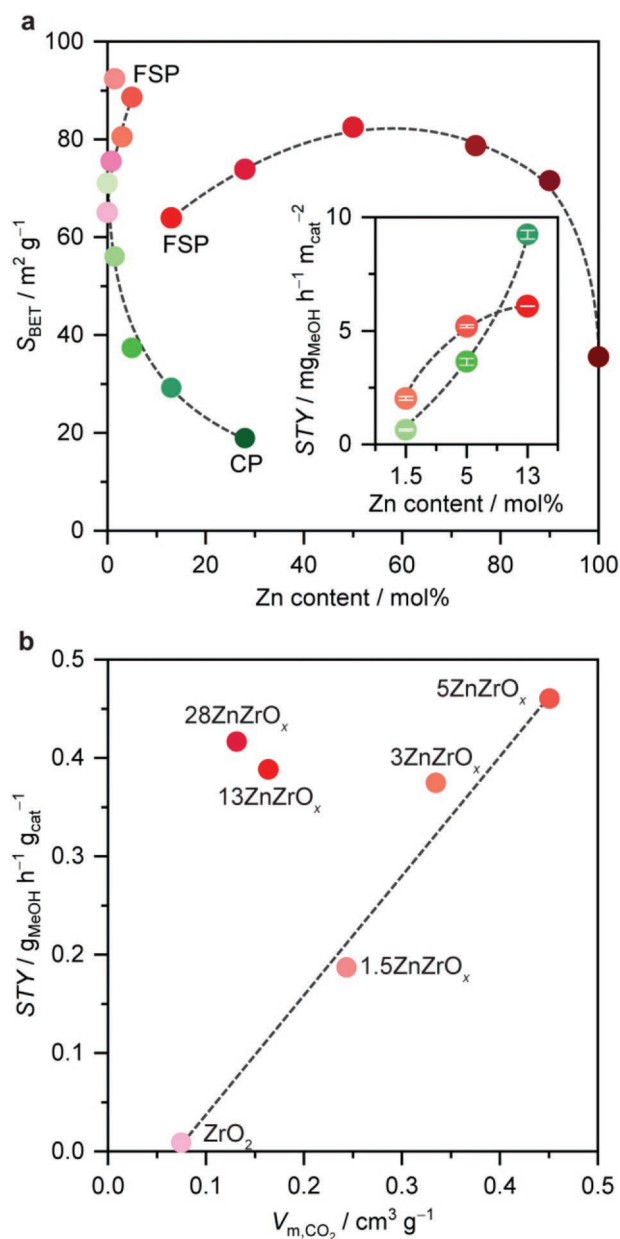
Figure 6. Correlation between a) Brunauer–Emmet–Teller (BET) surface area (S_{BET}) and zinc content, and b) methanol space-time yield (STY) and volumetric CO$_2$ uptake (V_{m,CO_2}) of flame spray pyrolysis (FSP) made ZnZrO$_x$ systems. Inset depicts methanol STY of selected coprecipitated (CP) and FSP catalysts normalized by their corresponding S_{BET}. Averaged values measured over 12 h on stream are presented with their corresponding error bars. Reaction conditions: T = 593 K, P = 5 MPa, H$_2$/CO$_2$ = 4, and gas hourly space velocity (GHSV) = 24 000 cm^3 h^{-1} g$_{cat}^{-1}$.

ZrO$_2$ polymorphs (Equations (S3) and (S4), Supporting Information). For this reason, supercells were used to simulate bulk phases (Figure S7, Supporting Information) whereas slab models of the most thermodynamically stable termination of each polymorph to assess surface and subsurface sites (Figures S7 and S8, Supporting Information).[36,37] A detailed discussion of all zinc incorporation sites and oxygen vacancies explored can be found in Section S1.2, Figures S10–S14, Supporting Information.
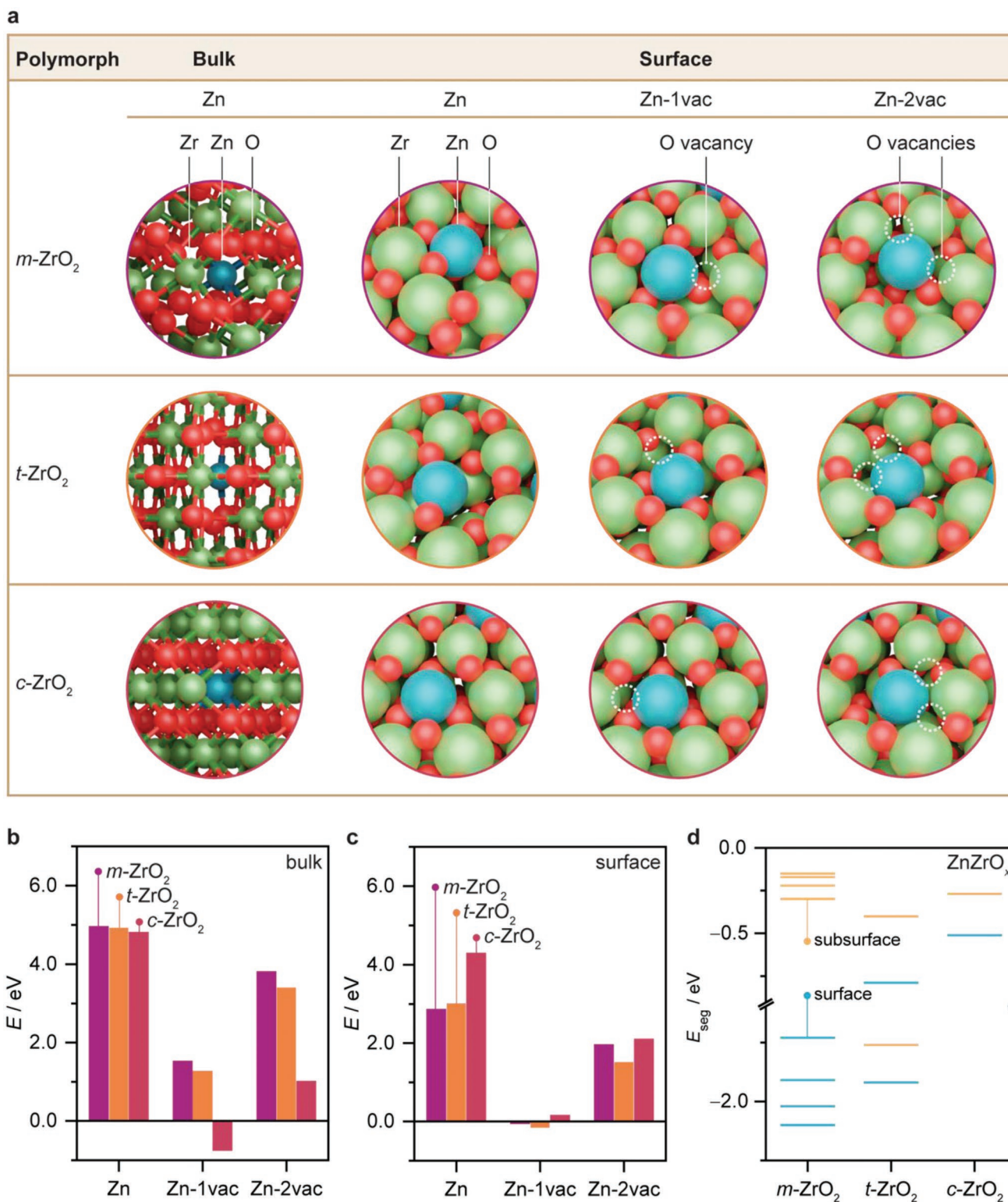
Figure 7. a) Density functional theory (DFT) models and potential energies (E) associated with the most stable structures with one incorporated zinc atom (Zn) and one (Zn-1vac) and two (Zn-2vac) oxygen vacancies at b) bulk and c) surface sites of monoclinic (m), tetragonal (t), and cubic (c) ZrO_2 polymorphs. d) Segregation energies (E_{seg}) for a zinc atom to move from bulk to surface and subsurface sites in distinct ZrO_2 polymorphs.

The incorporation of Zn to bulk sites is generally more favored for t-ZrO_2, and c-ZrO_2 compared to m-$ZnZrO_2$, and in all cases is accompanied by the formation of oxygen vacancies.

This explains the presence of t-ZrO_2 on CP systems even though it is less stable than m-ZrO_2 (**Figure 7**a,b, and Table S8, Supporting Information). Similarly, replacing Zr by Zn on the

most stable surfaces is fostered by the formation of vacancies and follows the same trend observed for bulk phases (Figure 7a,c, and Table S9, Supporting Information). These observations are further supported by the Raman spectra of fresh FSP catalysts, which contains t- and c-ZrO_2 phases on the surface (Figure 3b). Finally, Zn segregation energies (E_{seg}, Equation (S5), Supporting Information) show that surface sites are more thermodynamically stable compared to bulk positions for the three polymorphs, in particular for m-$ZnZrO_2$ (Figure 7d and Table S10, Supporting Information). This is in line with experimental findings showing that FSP induces preferential location of Zn atoms at the catalyst surface whereas bulk incorporation is favored by CP. In principle, the high temperatures experienced by materials during the FSP synthesis likely drive zinc toward occupying surface positions while the fast cooling rates, which is also characteristic of this synthesis method, assists on stabilizing such catalyst architecture, as previously reported for other systems.[38,39] Additionally, c-$ZnZrO_x$ exhibits the less favored segregation energies, which could also explain the formation of these phase on the catalyst surface only at high Zn contents (i.e., 13 mol%, Figure 3b).

2.3. Insights into the Vacancy Formation Mechanism

Oxygen vacancies (V_O) are common defects in reducible oxides and generally dictate their properties (Section S1.3, Figures S16–S18, Supporting Information). Nonetheless, despite their importance for promoting CO_2 conversion on $ZnZrO_x$ systems, there is still a lack of fundamental understanding of the formation and dynamics of such sites for this particular catalyst family.[40] For this reason, in situ electron paramagnetic spectroscopy (EPR) was applied to investigate the defect chemistry on the FSP $5ZnZrO_x$ and CP $13ZnZrO_x$ catalysts under practically relevant gaseous atmospheres (**Figure 8**a). As expected, the signal typically assigned to V_O is relatively weak for the fresh samples. When heated to 593 K in an inert atmosphere, a narrow and stronger isotropic signal (centered at $g = 2.003$) appears for both catalysts, whereas only $5ZnZrO_x$ shows an anisotropic feature at higher field with an axial g ($g_{xx} = g_{yy} = 1.977$, $g_{zz} = 1.959$). These signals are attributed to magnetically isolated unpaired electrons in oxygen vacancy ($V_O^\bullet$, electrons are represented by $\bullet$) and to reduced Zr atoms with one unpaired d electron (Zr^{3+}), respectively,[41–43] indicating that thermally induced vacancy generation predominates over FSP and CP catalysts. $V_O^\bullet$ and Zr^{3+} are formed by trapping the electrons which are released after the formation of an oxygen vacancy ($O_{lat}^{2-} \rightleftharpoons O_2 + 2e^-$).

By investigating oxygen vacancies in pure and Zn-containing ZrO_2 surfaces using DFT simulations (Figures S13 and S15, Supporting Information), we uncovered that $V_O^\bullet$–Zr^{3+} moieties (EPR active) are indeed more stable than $Vo^{\bullet\bullet}$–Zr^{4+} (EPR silent) by 0.04 eV (or 0.10 eV when calculated using a hybrid functional HSE03[44,45] with 13%[46] of nonlocal Hartree–Fock exchange, Figure 8b). Moreover, the simulations predict the preferential formation of $V_O^\bullet$–Zr^{3+} moieties over monoclinic zinc-free zirconia regions (Figure 8b). This behavior is in line with the stronger EPR signal observed for $5ZnZrO_x$ (Figure 8a), which
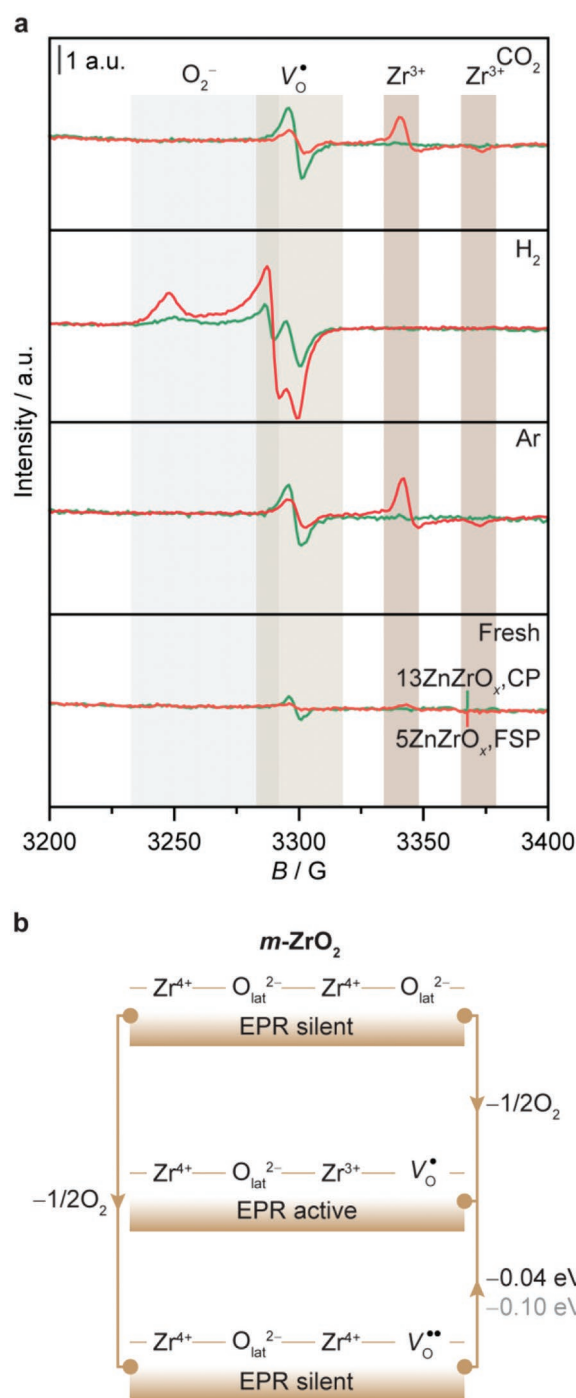
Figure 8. a) In situ electron paramagnetic spectroscopy (EPR) spectra of the flame spray pyrolysis (FSP) made $5ZnZrO_x$ and coprecipitated (CP) $13ZnZrO_x$ catalysts measured first under flowing Ar (100 min), followed by H_2 (100 min), and finally CO_2 (100 min). Activation conditions: $T = 593$ K, $P = 0.1$ MPa, $m_{cat} = 10$ mg, and flow(Ar) = flow(H_2) = flow(CO_2) = 20 cm³ min⁻¹. b) Oxygen vacancy formation mechanism for m-ZrO_2 showing EPR active and silent structures obtained by density functional theory (DFT) simulations (−0.04 and −0.10 eV (in gray) were obtained with the Perdew–Burke–Ernzerhof (PBE) and HSE03 functional, respectively).

ADVANCED
SCIENCE NEWS
www.advancedsciencenews.com

ADVANCED
ENERGY
MATERIALS
www.advenergymat.de

contains m-ZrO_2, and suggests that V_O located at the catalytic ensemble of $ZnZrO_x$ are likely not directly detected by EPR. Analysis of the vacancy formation energies (E_{vac}, Figure S9, Supporting Information), which indicate that generating V_O close to Zn atoms is significantly more favored than in zinc-free zirconia regions (Figure S15, Supporting Information), further supports this hypothesis. Indeed, the former structure is very exothermic in $ZnZrO_x$ for the three zirconia polymorphs ($E_{vac} = -3.06$, -4.42, and -3.93 for m-, t-, and c-$ZnZrO_x$, respectively), and thereby more relevant for catalytic purposes (Figure S19, Supporting Information). However, defect sites close to Zn result in EPR silent species ($Vo^{\bullet\bullet}$) and, thus, cannot be directly probed by EPR measurements.

In situ EPR measurements under H_2 feeds revealed the formation of superoxide species (O_2^-) on both samples, generating a characteristic anisotropic signal with an orthorhombic g ($g_{xx} = 2.007$, $g_{yy} = 2.014$, $g_{zz} = 2.041$, Figure 8a).[47] DFT simulations suggest that the O_2^- species are formed and stabilized owing to hydrogen incorporation into the oxygen vacancy (EPR silent, Figure S20a,b, Supporting Information). Specifically, zinc incorporation into the m-ZrO_2 lattice creates these vacancies and peroxide species, with the latter evolving into superoxo O_2^- species (EPR active) upon H_2 exposure (Figure S20b, Supporting Information). In principle, the O_2^- signals provide indirect information about the density of H_2-induced EPR silent V_O located at the catalyst ensemble of $ZnZrO_x$ systems. In fact, $13ZnZrO_x$,CP shows significantly weaker O_2^- signals than $5ZnZrO_x$ (Figure 8a), indicating that the latter promotes V_O formation substantially, which is in line with its superior methanol productivity. Additionally, Zr^{3+} signals disappear upon exposure to H_2, indicating that the excess electron associated with Zr^{3+} is either trapped in empty vacancies[41] or not localized at a single zirconium cation (Figure S20a, Supporting Information). Finally, under a CO_2-containing atmosphere, $V_O^{\bullet}$–Zr^{3+} signals recover due to the formation of H_2O from O_2^- species (Figure S20a, Supporting Information). Overall, $V_O^{\bullet}$, Zr^{3+}, and O_2^- EPR signals can be considered proxies to probe the total amount of oxygen vacancies generated over $ZnZrO_x$ systems.

2.4. Mechanism and Kinetic Modeling

To explain the reactivity of FSP and CP catalysts, energy profiles for methanol (CH_3OH) and CO formation were calculated for the three Zn-containing ZrO_2 polymorphs containing one oxygen vacancy (**Figure 9** and Figures S21–S24, Supporting Information). Since previous studies on $ZnZrO_x$,[10] and other oxides (i.e., In_2O_3[19] and metal-doped In_2O_3[18,24]) have shown that CO_2 hydrogenation to CH_3OH is more favored through the formate pathway, this route was selected to study all three ZrO_2 polymorphs. The process starts with CO_2 activation through chemisorption as carbonate with the two oxygens interacting with open Zr metal sites.[48] This step is followed by the heterolytic activation of molecular H_2 leading to a ZnH+OH pair. Then, the hydride is transferred to CO_2 to obtain formate (CHO_2), which is either subsequently protonated to form formic acid ($CHOOH$) or hydrogenated to CH_2O_2 following the heterolytic dissociation of a second H_2 molecule. The

second path is favored for the three polymorphs, in particular for t-$ZnZrO_x$ (Figures S25–S27, Supporting Information). The formation of CH_2O_2 is followed by its protonation to CH_2OOH and concomitant dehydration leading to CH_2O and H_2O. The transfer of a hydride and a proton, produced by dissociative activation of a third H_2 molecule, yields methanol. In contrast, the RWGS reaction to form CO starts with the protonation of CO_2 leading to a carboxylate (COOH), which is further protonated and dehydrated forming CO and H_2O. CH_3OH formation is favored over CO for the three polymorphs. Following this prediction and the stable methanol STY experienced by $5ZnZrO_x$ (FSP) and $13ZnZrO_x$ (CP) when evaluated in the hydrogenation of hybrid CO_2-CO feeds (60 h) containing equimolar ratios of both carbon feedstocks (Figure S28, Supporting Information), we can conclude that methanol formation through the CO route is very unlikely. Additionally, analysis of high-angle annular dark-field scanning transmission electron microscopy EDX (HAADF–STEM–EDX) images (Figure S29, Supporting Information) shows only slight zinc aggregation in $5ZnZrO_x$ (FSP) and $13ZnZrO_x$ (CP) samples retrieved after the long-term evaluation, consistent with their remarkable stable performance. This confirms that regardless of the synthesis method used, $ZnZrO_x$ catalysts possess remarkable robustness against feed composition fluctuations and overreduction by stronger reducing species such as CO, a common byproduct in CO_2 hydrogenation.

When comparing the three ZrO_2 polymorphs, their energy profiles show that key intermediates, such as CHO_2, CH_2O_2, CH_2OOH, and CH_3O, are overstabilized on t- and c-$ZnZrO_x$ (Figure 9 and Figure S21, Supporting Information). We attribute these differences to the local coordination of Zn in the active site of these polymorphs (Figure S30, Supporting Information). While Zn adopts a square planar geometry on m-$ZnZrO_x$, the coordination on t- and c-$ZnZrO_x$ is a distorted tetrahedra similar to the tetrahedral coordination of Zn in its bulk ZnO oxide. Additionally, oxygen atoms of the overstabilized intermediates interact with open Zr sites and some of them also with Zn. Therefore, we put forward the distinct acidity of surface metal cations as a key reason for differences in reactivity between m-$ZnZrO_x$ and the other two Zn-containing zirconia polymorphs (Section S1.4, Figure S31, Supporting Information).

A practical kinetic model was developed for the most active catalyst to link the DFT-derived insights on energetics and kinetic barriers over the active m-$ZnZrO_x$ polymorph at the atomic scale with reaction rates at the reactor level (Section S1.5, Supporting Information). To build the model we employed 93 experimental data points obtained from the results of CO_2 hydrogenation over the FSP-made $5ZnZrO_x$ at different T, P, gas hourly space velocity (GHSV), and H_2/CO_2 ratios. A Langmuir–Hinshelwood–Hougen–Watson (LHHW) mechanism was employed for modeling the adsorption, elementary surface reaction, and desorption steps corresponding to the DFT reaction mechanism (Figure 9). Three models were evaluated and compared assuming different rate-determining steps (rds A = step 2, B = step 4, and C = steps 4 + 5, Figure 9a) and a one-site mechanism (two species adsorbed on the same site, *, Table S12, Supporting Information). The latter offers the best fit to the data and hints that the lumped fourth and fifth
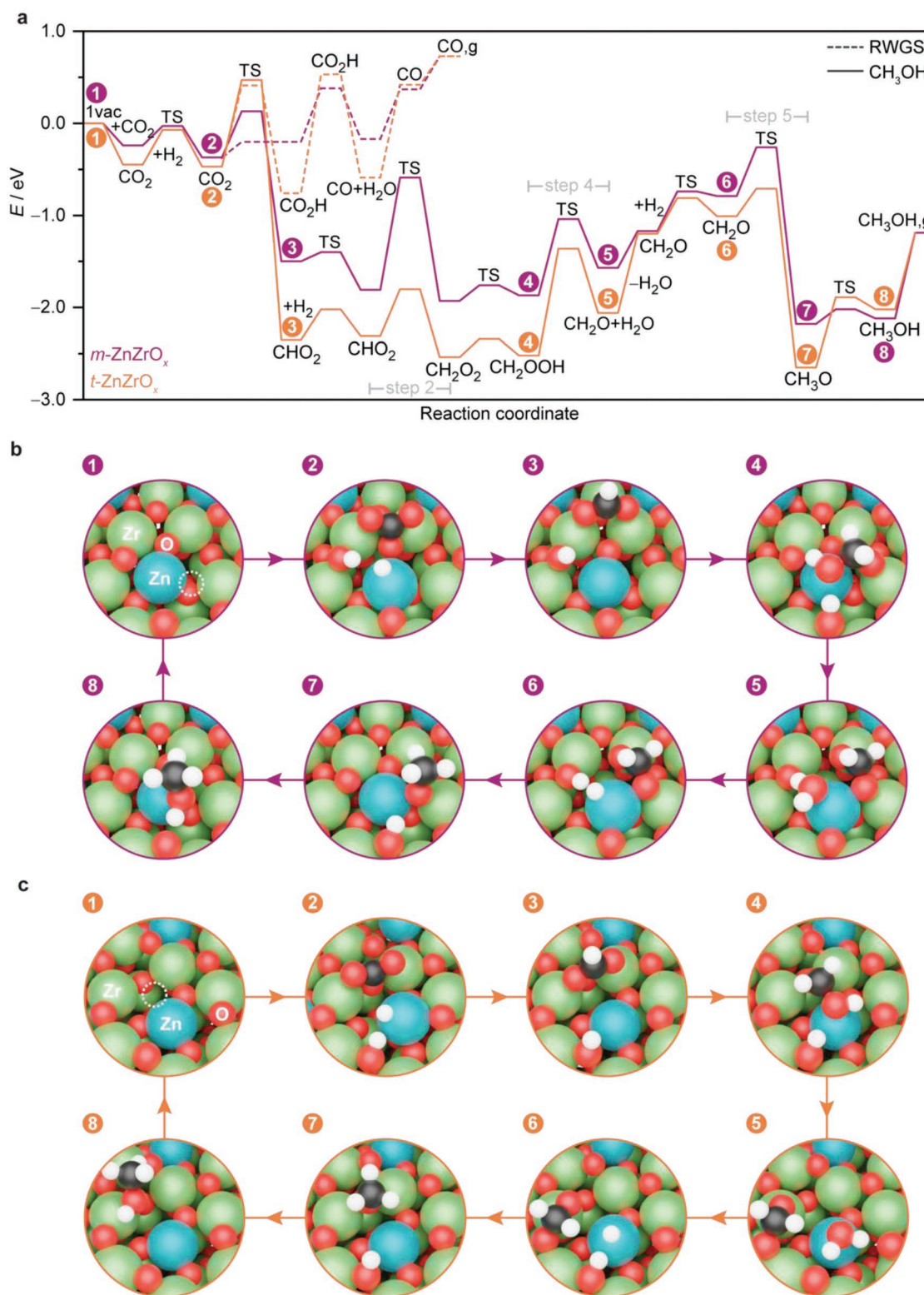
Figure 9. a) Reaction energy profiles for CO_2 hydrogenation to CH_3OH (solid line) and the competing RWGS reaction (dashed line) on m-$ZnZrO_x$ (purple) and t-$ZnZrO_x$ (orange) systems containing one oxygen vacancy. Intermediates labels (1–8) are the same for both systems. Snapshots of representative intermediates for b) m-$ZnZrO_x$ and c) t-$ZnZrO_x$ models. Color code: Zr (green), Zn (blue), O (red), C (dark gray), H (white), and oxygen vacancy (dotted white circles).

hydrogenation steps, combining those with the largest kinetic barrier (i.e., protonation of CH_2OOH* followed by dissociation to CH_2O* and H_2O*, and further hydrogenation of CH_2O* leading to CH_3O*, Figure 9) is the rds.

Moreover, DFT suggests a different adsorption site depending on the intermediate pointing to a two-site mechanism (two species adsorbed on different sites, * and #). However, including this atomistic detail brings no statistical improvement in the model (**Figure 10**a,b and Tables S12 and S13, Supporting Information). This is because the two-site mechanism assumes that both sites behave as totally independent variables, but the number of vacancies (required for CO_2 trapping) and available oxygens (useful in H_2 activation) are interdependent (i.e., if a vacancy is present H_2 cannot be activated and vice versa). Thus, spatially resolved adsorption sites does not directly mean that their site counting is directly uncoupled. Then, the one-site model C was used to obtain the expressions and fitted parameters for the MeOH formation and RWGS reactions (Table S13, Supporting Information). From the overall rate constants, the apparent activation energies of the MeOH formation and the RWGS reaction pathways are 109.7 and 124.5 kJ mol^{-1}, respectively, in line with experimental observations as well as DFT simulations that CO formation has a higher activation barrier while methanol formation is comparatively favorable. As for other catalysts methanol and water desorption steps have significant barriers but not limiting.
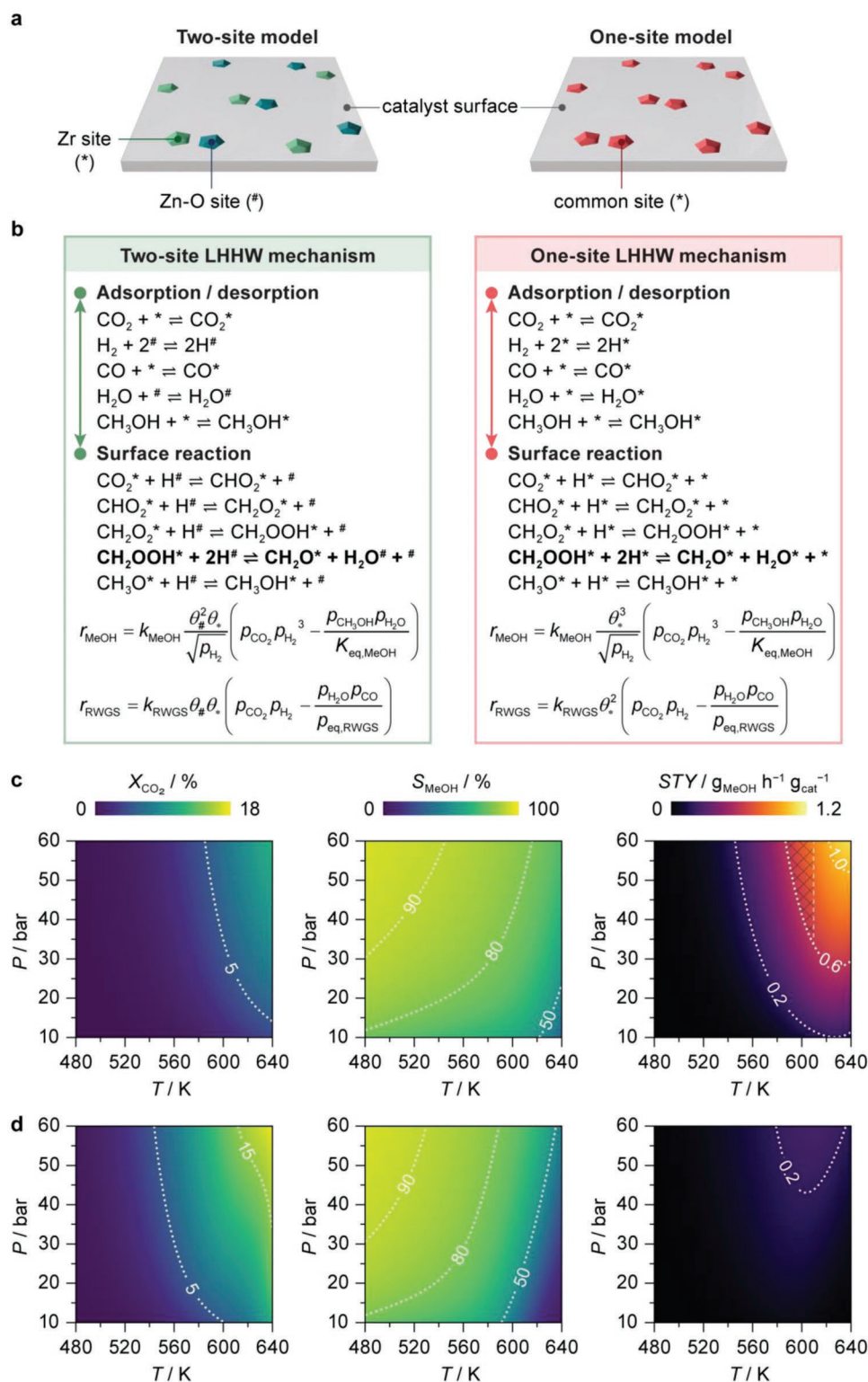
Model predictions of single-pass X_{CO_2}, S_{MeOH}, and methanol STY are plotted in Figure 10c,d for a reactor operating in a process-relevant temperature and pressure range under continuous flow at high and low space velocities. At GHSV = 8000 cm^3 h^{-1} g$_{cat}$$^{-1}$, overall CO_2 conversion approaches the limit dictated by thermodynamic equilibrium, at the expense of low S_{MeOH}. On the other hand, at GHSV = 48 000 cm^3 h^{-1} g$_{cat}$$^{-1}$, the reaction is kinetically controlled as X_{CO_2} remains below 5% at temperatures lower than 600 K with higher S_{MeOH}, as well as superior methanol STY theoretically exceeding 1 g$_{MeOH}$ h^{-1} g$_{cat}$$^{-1}$ at sufficient pressures. Based solely on thermodynamic arguments, one could imagine using FSP catalysts at lower temperatures but higher pressures. However, since hydrogen activation, and related oxygen vacancy formation, are limited at lower temperatures, methanol productivity also decreases with this parameter. Since S_{MeOH} is still relatively high at 593 K and 50 bar (≈80%, Table S2, Supporting Information), it would not significantly improve by decreasing the operating temperatures. Indeed, the ideal operating window for maximizing single-pass MeOH yield, considering also catalyst deactivation which becomes significant when operating at extremely high temperatures, lies around 580–610 K. This is a higher temperature range than that for In_2O_3-based catalysts, and in turn higher than that for Cu-based catalysts. The positive variation of all performance indicators with increasing P, as well as the trade-off between X_{CO_2} with S_{MeOH} with changing T and GHSV, are evident trends common to CO_2-to-methanol over different MeOH synthesis catalysts.

Overall, the catalyst surface area noticeably impacts the performance difference between FSP and CP systems, but it is not the only factor. FSP also improves zinc utilization and maximizes its location and atomic dispersion at surface lattice positions of the ZrO_2 phase, which is also critical for obtaining improved methanol productivity. Additionally, FSP is a scalable and one-step preparation method, which requires no postsynthetic treatments such as washing and calcination steps. Still, FSP and CP catalysts containing atomically dispersed zinc species possess identical active ensembles, which comprise an oxygen vacancy and neighboring zinc, zirconium, and an oxygen associated with zirconium atoms. Due to their intricate and dynamic nature, estimating the number of active ensembles requires determination of both the density of oxygen vacancies and surface Zn dispersion under operando conditions. However, methodologies for quantifying these parameters are lacking, which hinders the calculation of turnover frequencies of both FSP and CP catalysts and, therefore, should be tackled in future studies.

3. Conclusions

In summary, we presented $ZnZrO_x$ catalysts attained by a one-step FSP method and featuring improved zinc utilization that significantly outperform the state-of-the-art coprecipitated systems in CO_2 hydrogenation to methanol, especially with Zn contents up to 5 mol%. The holistic approach integrating catalytic evaluation, in-depth characterization, DFT simulations, and kinetic modeling permitted a thorough comparison of FSP and CP catalysts and hence derive detailed synthesis–structure–performance relationships. In general, methanol productivity is boosted over systems containing a high concentration of atomically dispersed Zn^{2+} sites doped at lattice positions within the ZrO_2 surface, which is present on both FSP and CP catalysts and was identified as their common catalytic ensemble. However, unlike CP, FSP grants materials with enhanced surface area (60–90 versus 20–50 m^2 g^{-1}), owing to its ability to maximize isolated surface Zn^{2+} species without inducing zinc incorporation into the bulk phase of the ZrO_2 carrier, a common feature of CP that negatively impacts textural properties of $ZnZrO_x$ materials. In addition, the unique architecture of the flame-made catalyst facilitates the creation of oxygen vacancies upon reaction, as evidenced by in situ EPR spectroscopy. DFT simulations further elucidated that $V_O^\bullet$, Zr^{3+}, and O_2^- EPR fingerprints used to probing the vacancy dynamics, act as proxy to also detecting defects close to the Zn^{2+} sites, which are more easily formed than those next to Zr^{4+} ions but are generally EPR silent. More importantly, active ensembles comprising an oxygen vacancy and neighboring zinc, zirconium, and an oxygen associated with zirconium atoms markedly foster methanol formation through the formate path, particularly for zinc-doped monoclinic ZrO_2, while hindering CO production. Finally, kinetic analyses enabled the development of models with significant predictive power of the catalytic performance at process-relevant conditions. Overall, this study advances the atomic-level understanding of $ZnZrO_x$ catalytic systems, and offers a promising design and practical guidelines for their implementation in methanol production from CO_2. The FSP approach reported can also potentially revitalize research efforts toward more sustainable and efficient heterogeneous catalytic materials for diverse energy-related applications.

Figure 10. a) Schematic representation of the two- and one-site kinetic models, depicted on the left and right, respectively. b) Elementary steps and rate expressions for the two model variants with the rate-determining step (rds, which results from the lumped fourth and fifth hydrogenation steps depicted in Figure 9a. That is, the protonation of CH_2OOH^* followed by dissociation to CH_2O^* and H_2O^*, and the hydrogenation of CH_2O^* leading to CH_3O^*) marked in bold. The one-site model predictions of overall CO_2 conversion, methanol selectivity, and methanol space-time yield (STY) for CO_2 hydrogenation over the 5ZnZrO$_x$ catalyst prepared by flame spray pyrolysis (FSP) as a function of reaction temperature and total pressure, at c) high and d) low space velocities. Reaction conditions: $H_2/CO_2 = 4$, and c) gas hourly space velocity (GHSV) = 48 000 cm^3 h^{-1} g$_{cat}^{-1}$, d) GHSV = 8000 cm^3 h^{-1} g$_{cat}^{-1}$. Dotted contour lines show values referenced in the discussion as a guide for readers.

4. Experimental Section

Catalyst Synthesis-Flame Spray Pyrolysis: ZnZrO$_x$ catalysts with a Zn content ranging from 0 to 100 mol% were synthetized by FSP (denoted as ZnZrO$_x$). Zinc(II) and zirconium(IV) 2-ethylhexanoate in the desired molar ratio were dissolved in 2-ethylhexanoate and tetrahydrofuran (EHA/THF mass ratio of 2:1) to yield a 5.9 wt% solution of Zn:Zr equivalents. The precursor solution was then injected into a 0.4 mm nozzle at a flow rate of 5 L min^{-1}, where it was dispersed by a 5 L min^{-1} stream of oxygen at 1.5 bar. Pilot flames sustained by a 2:1 oxygen/methane feed at 3.6 L min^{-1} ensured ignition of the spray. Such conditions have been reported to generate average flame temperature of 2500–3000 K.[23,49,50] The resulting nanoparticles were collected on a glass fiber filter (GF/A-6) and used in CO$_2$ hydrogenation without further treatment.

Catalysts with a molar zinc content ranging from 1.5 to 28 mol% (denoted as ZnZrO$_x$,CP) were prepared by coprecipitation, based on a reported procedure.[10] The method is described for a zinc content of 13 mol%. Briefly, zinc nitrate hexahydrate (1.3 g, Zn(NO$_3$)$_2$·6H$_2$O, Sigma–Aldrich, >99%) and zirconil chloride octahydrate (9.7 g, ZrOCl$_2$·8H$_2$O, Sigma–Aldrich, 98%) were dissolved in deionized water (200 cm^3). Separately, ammonium carbonate (6.4 g, (NH$_4$)$_2$CO$_3$, Sigma–Aldrich, >30% NH$_3$ basis) was dissolved in deionized water (200 cm^3). The precipitant solution was added dropwise to the precursor solution at 343 K under magnetic stirring (≈500 rpm) until reaching pH 8. After 2 h of aging in the same conditions, the resulting suspension was cooled down to room temperature. The precipitant was then recovered by centrifugation (6000 rpm, 5 min), washed four times with deionized water (240 cm^3 each time), dried in a vacuum oven (2 kPa, 333 K, 12 h), and calcined for 3 h in static air at 773 K (2 K min^{-1}).

Catalyst Characterization: X-ray fluorescence spectroscopy (XRF) was performed using an Orbis Micro-EDXRF spectrometer equipped with a Rh source operated at 35 kV and 500 µA and a silicon drift detector. Nitrogen sorption at 77 K was carried out using a Micromeritics TriStar II analyzer. Prior to the measurements, samples were degassed at 473 K under vacuum for 12 h. The total surface area (S_{BET}) was determined using the Brunauer-Emmet-Teller (BET) method. XRD was conducted using a Rigaku SmartLab diffractometer with a D/teX Ultra 250 detector using Cu Kα radiation (λ = 0.1541 nm) and operating in the Bragg–Brentano geometry. Data was acquired in the 20–70° 2θ range with an angular step size of 0.025° and a counting time of 1.5 s per step. HAADF–STEM and HRTEM images and EDX spectroscopy maps were collected using a Talos F200X instrument operated at an acceleration potential of 200 kV. Samples were dusted on lacey-carbon coated copper grids. Raman spectroscopy was performed using a Horiba: LabRAM HR Evolution UV-VIS-NIR confocal Raman system comprising a 325 nm HeCd laser with 2.5 mW power, a 40× objective lens with a numerical aperture of 0.95 (Nikon PlanApo), and a fiber coupled grating spectrometer (1800 lines per mm). Spectra were collected in a single run with 60 s acquisition time. For data evaluation, the intensities were normalized to the highest measured intensity after subtraction of a linear background. XPS was performed using a Physical Electronics (PHI) Quantum 2000 X-ray photoelectron spectrometer featuring monochromatic Al Kα radiation, generated from an electron beam operated at 15 kV and 32.3 W, and a hemispherical capacitor electron-energy analyzer, equipped with a channel plate and a position-sensitive detector. Samples were firmly pressed onto aluminum foil, which was then mounted onto a sample platen and introduced into the spectrometer. Analyses were conducted under ultra-high vacuum (residual pressure = 6 × 10^{-9} Pa) with an electron take-off angle of 45°, operating the analyzer in the constant pass energy mode. X-ray absorption spectroscopy (XAS) was measured at at the Swiss–Norwegian beamlines (SNBL, BM31) at the European Synchrotron Radiation Facility (ESRF).[51] The energy was selected by a double-crystal Si(111) monochromator,[51] and calibrated using a Zn foil (9.6586 keV), which was measured simultaneously with the specimen of interest. The incident X-ray beam was focused on a 0.25 × 1 mm^2 spot. Activated samples (T = 593 K, P = 5 MPa, H$_2$/CO$_2$ = 4, GHSV = 24 000 cm^3 h^{-1} g$_{cat}^{-1}$,

and TOS = 20 h) were transferred from the reactor to a quartz capillary and sealed under inert atmosphere. Reference ZnO was measured in transmission mode as a pellet diluted with cellulose. Three 15-cm long ionization chambers filled with 50 vol% N$_2$ in Ar at 2 bar were used to monitor the incident beam intensity, transmission through the sample, and the reference foil. The XAS spectra of 5 and 13ZnZrO$_x$ samples were measured using a fluorescence detection mode using a 5-element SDD detector (SGX) and step-by-step data acquisition mode. The spectra were calibrated and averaged with the in-house developed ProEXAFS software and further analyzed using the Demeter software package.[52] k^3-weighted EXAFS spectra were fitted in the optimal k- and R-windows (Table S6, Supporting Information). An amplitude reduction factor (S_0^2) of 1.2 was determined by fitting of the EXAFS spectrum of a Zn foil. The scattering paths for the fitting were produced using known crystallographic structures of metallic Zn and hexagonal ZnO. In situ electron paramagnetic resonance EPR spectroscopy experiments were performed using a custom-built setup (microwave frequency = 9.2 GHz, center field = 300 mT, sweep width = 570 mT, modulation amplitude = 3 G, modulation frequency = 100 kHz, microwave power = 1.986 mW, power attenuation = 20 dB, conversion time = 86.55 ms, time constant = 20.48 ms.). A quartz capillary (d_i = 0.8 mm) was loaded with the catalyst, and placed inside an EPR quartz tube (Wilmad; d_i = 2.8 mm). The EPR tube was placed at the center of a homemade water-cooled high-temperature resonator,[53] which was installed into a continuous wave EPR spectrometer (Bruker EMX) operating at X-band frequencies. The gas flow was directed from the top of the capillary through the catalyst bed and then through the space between the capillary outer walls and the EPR tube inner walls. The reactor was heated in an Ar flow to the desired temperature (T = 593 K) and allowed to stabilize for 20 min. The two reactant gases were sequentially admitted to the reactor, i.e., a H$_2$ (20 cm^3 min^{-1}) was kept flowing for 2 h, followed by CO$_2$ (20 cm^3 min^{-1}) for 2 h. The gases were dosed by a set of digital mass flow controllers and the outcome was monitored online via a Pfeiffer Vacuum Thermo-Star GSD 320 T1 mass spectrometer. The EPR spectra were continuously acquired upon flowing the gases and separately stored, using a 2D acquisition mode, thus enabling a time-resolved monitoring of the process.

Catalyst Evaluation: The gas-phase hydrogenation of CO$_2$ to methanol was performed in a PID Eng&Tech high-pressure continuous-flow setup comprising four parallel fixed-bed reactors, as described elsewhere.[54] Undiluted catalysts (mass, m_{cat} = 0.1 g; particle size = 0.2–0.4 mm) were loaded into each reactor tube (internal diameter 4 mm), held in place by a quartz-wool bed set on a quartz frit, and purged in flowing He (40 cm^3 min^{-1}, PanGas, 4.6) for 30 min at ambient pressure. Under the same flow, the pressure was increased to 5.5 MPa for a leak test. The reaction was carried out by feeding a mixture of H$_2$ (PanGas, 5.0), CO$_2$ (40 vol% in H$_2$, Messer, 4.5), and, in the case of hybrid feeds, also CO (Messer, 5.0), with a molar H$_2$/CO$_x$ (CO$_x$ = CO$_2$ + CO) ratio of 4 at 593 K, 5 MPa, and GHSV of 24 000 cm^3 h^{-1} g$_{cat}^{-1}$, unless stated otherwise. The selectivity of the catalysts was compared at a constant degree of CO$_2$ conversion (X_{CO_2}) as described in Figure 2 by adjusting the GHSV for each system. Further catalyst evaluation data points used in the fitting and validation of the kinetic model were obtained in a secondary self-built continuous flow setup equipped with a single fixed-bed reactor of 2.2 mm internal diameter, as described elsewhere.[19] The full list of conditions (T, P, H$_2$/CO$_2$, GHSV, and m_{cat}) can be viewed the supplementary Excel file found in the Zenodo repository (https://doi.org/10.5281/zenodo.7359881). The testing procedure and quantification calculations are identical to those for the parallel reactor setup and give the same results within 5% error.

The effluent streams were analyzed by gas chromatography every 1 h and 15 min for the parallel and single setups, respectively. Response factors (F_i) for each compound i, respective to the internal standard (20 vol% C$_2$H$_6$ in He, Messer, purity 3.5), in the GC analysis were determined by Equation (1):

$$F_i = \frac{A_{C_2H_6}/n_{C_2H_6}^{in}}{A_i/n_i^{in}} \tag{1}$$

**ADVANCED
SCIENCE NEWS**

www.advancedsciencenews.com

**ADVANCED
ENERGY
MATERIALS**

www.advenergymat.de

where A_i is the integrated area determined for the peak of compound i and n_{in} is the corresponding known molar flow at the reactor inlet. An average of five points around the expected analyte concentration was used. The unknown effluent molar flow of compound i was determined using Equation (2):

$$n_i^{out} = \frac{A_i \times F_i}{A_{C_2H_6}} \times n_{C_2H_6}^{out} \tag{2}$$

Conversion (X_i), selectivity (S_i), and production rate (r_i) were calculated using Equations (3)-(5):

$$X_i = \frac{n_i^{in} - n_i^{out}}{n_i^{in}} \tag{3}$$

$$S_i = \frac{n_i^{in} - n_i^{out}}{n_{CO_2}^{in} - n_{CO_2}^{out}} \tag{4}$$

$$r_i = \frac{n_i^{in} - n_i^{out}}{m_{cat}} \tag{5}$$

The methanol space-time yield (STY) is the product of r_{MeOH} and the molar weight of methanol (32.04 g mol^{-1}). The carbon balance was determined for each experiment according to Equation (6):

$$\varepsilon_C = \left(1 - \frac{n_{CO_2}^{out} + n_{MeOH}^{out} + n_{CO}^{out}}{n_{CO_2}^{in}}\right) \tag{6}$$

and was always within a 5% margin.

Theoretical Simulations: DFT simulations were carried out with Vienna ab initio simulation package (VASP),[55,56] employing the Perdew–Burke–Ernzerhof (PBE) density functional.[57] Valence electrons were expanded with plane-waves with a kinetic cut-off energy of 500 eV while core electrons were described by projector augmented wave (PAW) pseudopotentials.[58] The Brillouin zone was sampled by a Γ-centered mesh with a reciprocal grid size narrower than 0.037 Å^{-1}, generated with the Monkhorst–Pack method.[59]

Bulk lattice parameters of three ZrO_2 polymorphs were optimized with a kinetic energy cut-off of 700 eV. The three polymorphs are monoclinic (*m*), tetragonal (*t*), and cubic (*c*), which belongs to *P2₁/c*, *P4₂/nmc,* and *Fm$\overline{3}$m* space groups, respectively. The calculated lattice parameters are in good agreement with experiments and previous theoretical studies (Table S7, Supporting Information).[36,60–63] The presence of Zn on the three polymorphs was assessed by replacing one Zr atom in $2 \times 2 \times 2$ (monoclinic and cubic) and $2 \times 2 \times 3$ (tetragonal) supercells (Figure S7a (Supporting Information) and Section S1.2.2, Supporting Information). These supercells were also used to explore oxygen vacancy formation, both in the undoped and Zn-doped ZrO_2 systems. See Section S1.2.2 (Supporting Information) for a detailed explanation of the oxygen selected to form the vacancies.

Periodic boundary conditions were employed to model oxygen terminated slabs representing the most stable surface of each polymorph, which are (–111), (101), and (111) for *m*-, *t*-, and *c*-ZrO_2, respectively.[36,37] In all cases, the slabs contained four layers being the two bottom ones fixed to bulk positions and the two outermost were allowed to relax. A vacuum region of 15 Å between slabs and a dipole correction along the *z* axes was applied in the three models.[64] The morphology of each polymorph is different, and their models were accordingly built (Figure S7b, Supporting Information). *m*-ZrO_2 (–111) was modeled as a *p*(1 × 1) slab where each of the four layers is composed by four ZrO_2 formula units grouped in 12 atomic layers (O–O–O–Zr–O–Zr–Zr–O–Zr–O–O–O). *t*-ZrO_2 (101) was represented with a *p*(1 × 2) slab with each layer formed by five atomic layers (O–O–Zr₂–O–O) and 4 ZrO_2 formula units. Finally, *c*-ZrO_2(111) was built as *p*(2 × 2) slab where each layer contains three atomic layers (O–Zr–O).

with four ZrO_2 formula units. Overall, the slabs for the three ZrO_2 polymorphs contain the same number of layers, ZrO_2 formula units, and ratio of relaxed/fixed atoms, although the Zr-O motifs are different (Figure S7b and Section S1.2.3, Supporting Information). The presence of Zn on the three surfaces was evaluated by replacing each of the non-equivalent Zr atoms of the two outermost layers (surface and subsurface), as depicted in Figure S8 (Supporting Information). The formation of oxygen vacancies was also assessed on the undoped and Zn-doped ZrO_2 slab models (Figure S9, Supporting Information). See Section S1.2.3 (Supporting Information) for a detailed explanation of the oxygen selected to form the vacancies. In addition, single points of relevant structures for the discussion of the oxygen vacancy formation and its link to EPR results were carried out with a hybrid functional HSE03[44,45] with 13%[46] of nonlocal Hartree–Fock exchange. Energy profiles for CO_2 hydrogenation to CH_3OH and the competitive RWGS were computed on the $ZnZrO_x$ models of the three polymorphs with one Zn replacing a Zr atom on surface sites and one oxygen vacancy. The Zn doped surfaces with one vacancy, CO_2, H_2, and H_2O were employed as thermodynamic sinks. Transition states were located using the climbing image nudged elastic band (CI-NEB) method.[65] The nature of transitions states was confirmed by computing numerical frequencies with a step size of ± 0.015 Å.

Supporting Information

Supporting Information is available from the Wiley Online Library or from the author.

Acknowledgements

Conflict of Interest

The authors declare no conflict of interest.

Data Availability Statement

The data that support the findings of this study are openly available in Zenodo at https://doi.org/10.5281/zenodo.7359881, reference number 7359881.[66] Inputs and outputs for all DFT simulations can be found online in the ioChem-BD repository[67,68] at http://doi.org/10.19061/iochem-bd-1-259.

[1] K. Narine, J. Mahabir, N. Koylass, N. Samaroo, S. Singh-Gryzbon, A. Baboolal, M. Guo, K. Ward, *J. CO₂ Util.* **2021**, *44*, 101399.

[2] J. Sehested, *J. Catal.* **2019**, *371*, 368.

[3] L. Van Hoecke, L. Laffineur, R. Campe, P. Perreault, S. W. Verbruggen, S. Lenaerts, *Energy Environ. Sci.* **2021**, *14*, 815.

[4] M. Erans, E. S. Sanz-Pérez, D. P. Hanak, Z. Clulow, D. M. Reiner, G. A. Mutch, *Energy Environ. Sci.* **2022**, *15*, 1360.

[5] A. González-Garay, M. S. Frei, A. Al-Qahtani, C. Mondelli, G. Guillén-Gosálbez, J. Pérez-Ramírez, *Energy Environ. Sci.* **2019**, *12*, 3425.

[6] G. A. Olah, A. Goeppert, G. K. S. Prakash, *Beyond Oil Gas*, Wiley, Weinheim, Germany **2018**, p. 205, https://doi.org/10.1002/9783527805662.ch10.

[7] X. Jiang, X. Nie, X. Guo, C. Song, J. G. Chen, *Chem. Rev.* **2020**, *120*, 7984.

[8] J. Zhong, X. Yang, Z. Wu, B. Liang, Y. Huang, T. Zhang, *Chem. Soc. Rev.* **2020**, *49*, 1385.

[9] M. Suvarna, T. P. Araújo, J. Pérez-Ramírez, *Appl. Catal., B* **2022**, *315*, 121530.

[10] J. Wang, G. Li, Z. Li, C. Tang, Z. Feng, H. An, H. Liu, T. Liu, C. Li, *Sci. Adv.* **2017**, *3*, e1701290.

[11] K. Li, J. G. Chen, *ACS Catal.* **2019**, *9*, 7840.

[12] Z. Han, C. Tang, F. Sha, S. Tang, J. Wang, C. Li, *J. Catal.* **2021**, *396*, 242.

[13] J. Wang, C. Tang, G. Li, Z. Han, Z. Li, H. Liu, F. Cheng, C. Li, *ACS Catal.* **2019**, *9*, 10253.

[14] T. P. Araújo, A. H. Hergesell, D. Faust-Akl, S. Büchele, J. A. Stewart, C. Mondelli, J. Pérez-Ramírez, *ChemSusChem* **2021**, *14*, 2914.

[15] J. Ding, Z. Li, W. Xiong, Y. Zhang, A. Ye, W. Huang, *Appl. Surf. Sci.* **2022**, *587*, 152884.

[16] M. S. Frei, C. Mondelli, A. Cesarini, F. Krumeich, R. Hauert, J. A. Stewart, D. Curulla Ferré, J. Pérez-Ramírez, *ACS Catal.* **2020**, *10*, 1133.

[17] B. Bachiller-Baeza, I. Rodriguez-Ramos, A. Guerrero-Ruiz, *Langmuir* **1998**, *14*, 3556.

[18] M. S. Frei, C. Mondelli, R. García-Muelas, K. S. Kley, B. Puértolas, N. López, O. V. Safonova, J. A. Stewart, D. Curulla Ferré, J. Pérez-Ramírez, *Nat. Commun.* **2019**, *10*, 3377.

[19] M. S. Frei, M. Capdevila-Cortada, R. García-Muelas, C. Mondelli, N. López, J. A. Stewart, D. Curulla Ferré, J. Pérez-Ramírez, *J. Catal.* **2018**, *361*, 313.

[20] T. Pinheiro Araújo, C. Mondelli, M. Agrachev, T. Zou, P. O. Willi, K. M. Engel, R. N. Grass, W. J. Stark, O. V. Safonova, G. Jeschke, S. Mitchell, J. Pérez-Ramírez, *Nat. Commun.* **2022**, *13*, 5610.

[21] W. Y. Teoh, R. Amal, L. Mädler, *Nanoscale* **2010**, *2*, 1324.

[22] E. K. Athanassiou, R. N. Grass, W. J. Stark, *Aerosol Sci. Technol.* **2010**, *44*, 161.

[23] R. Koirala, S. E. Pratsinis, A. Baiker, *Chem. Soc. Rev.* **2016**, *45*, 3053.

[24] T. Pinheiro Araújo, J. Morales-Vidal, T. Zou, R. García-Muelas, P. O. Willi, K. M. Engel, O. V. Safonova, D. Faust Akl, F. Krumeich, R. N. Grass, C. Mondelli, N. López, J. Pérez-Ramírez, *Adv. Energy Mater.* **2022**, *12*, 2103707.

[25] J. Chevalier, L. Gremillard, A. V. Virkar, D. R. Clarke, *J. Am. Ceram. Soc.* **2009**, *92*, 1901.

[26] C. Yang, C. Pei, R. Luo, S. Liu, Y. Wang, Z. Wang, Z. J. Zhao, J. Gong, *J. Am. Chem. Soc.* **2020**, *142*, 19523.

[27] H. Kim, K. M. Kosuda, R. P. Van Duyne, P. C. Stair, *Chem. Soc. Rev.* **2010**, *39*, 4820.

[28] M. Li, Z. Feng, G. Xiong, P. Ying, Q. Xin, C. Li, *J. Phys. Chem. B* **2001**, *105*, 8107.

[29] M. Li, Z. Feng, P. Ying, Q. Xin, C. Li, *Phys. Chem. Chem. Phys.* **2003**, *5*, 5326.

[30] T. L. Weiss, H. J. Chun, S. Okada, S. Vitha, A. Holzenburg, J. Laane, T. P. Devarenne, *J. Biol. Chem.* **2010**, *285*, 32458.

[31] S. Tada, K. Larmier, R. Büchel, C. Copéret, *Catal. Sci. Technol.* **2018**, *8*, 2056.

[32] C. Li, M. Li, *J. Raman Spectrosc.* **2002**, *33*, 301.

[33] D. Salusso, E. Borfecchia, S. Bordiga, *J. Phys. Chem. C* **2021**, *125*, 22249.

[34] P. Šot, G. Noh, I. C. Weber, S. E. Pratsinis, C. Copéret, *Helv. Chim. Acta* **2022**, *105*, 202200007.

[35] L. Mädler, H. K. Kammler, R. Mueller, S. E. Pratsinis, *J. Aerosol Sci.* **2002**, *33*, 369.

[36] C. Ricca, A. Ringuedé, M. Cassir, C. Adamo, F. Labat, *J. Comput. Chem.* **2015**, *36*, 9.

[37] A. Christensen, E. A. Carter, *Phys. Rev. B* **1998**, *58*, 8050.

[38] S. Loher, W. J. Stark, M. Maciejewski, A. Baiker, S. E. Pratsinis, D. Reichardt, F. Maspero, F. Krumeich, D. Günther, *Chem. Mater.* **2005**, *17*, 36.

[39] J. A. Kemmler, S. Pokhrel, J. Birkenstock, M. Schowalter, A. Rosenauer, N. Bârsan, U. Weimar, L. Mädler, *Sens. Actuators, B* **2012**, *161*, 740.

[40] K. Lee, U. Anjum, T. P. Araújo, C. Mondelli, Q. He, S. Furukawa, J. Pérez-Ramírez, S. M. Kozlov, N. Yan, *Appl. Catal., B* **2022**, *304*, 120994.

[41] C. Gionco, M. C. Paganini, E. Giamello, R. Burgess, C. Di Valentin, G. Pacchioni, *Chem. Mater.* **2013**, *25*, 2243.

[42] E. V. Frolova, M. I. Ivanovskaya, *Mater. Sci. Eng., C* **2006**, *26*, 1106.

[43] H. Liu, L. Feng, X. Zhang, Q. Xue, *J. Phys. Chem.* **1995**, *99*, 332.

[44] J. Heyd, G. E. Scuseria, M. Ernzerhof, *J. Chem. Phys.* **2003**, *118*, 8207.

[45] J. Heyd, G. E. Scuseria, M. Ernzerhof, *J. Chem. Phys.* **2006**, *124*, 219906.

[46] F. S. Hegner, D. Cardenas-Morcoso, S. Giménez, N. López, J. R. Galan-Mascaros, *ChemSusChem* **2017**, *10*, 4552.

[47] E. Giamello, M. Volante, B. Fubini, F. Geobaldo, C. Morterra, *Mater. Chem. Phys.* **1991**, *29*, 379.

[48] S. Kouva, J. Andersin, K. Honkala, J. Lehtonen, L. Lefferts, J. Kanervo, *Phys. Chem. Chem. Phys.* **2014**, *16*, 20650.

[49] A. J. Gröhn, S. E. Pratsinis, A. Sánchez-Ferrer, R. Mezzenga, K. Wegner, *Ind. Eng. Chem. Res.* **2014**, *53*, 10734.

[50] R. N. Grass, S. Tsantilis, S. E. Pratsinis, *AIChE J.* **2006**, *52*, 1318.

[51] W. van Beek, O. V. Safonova, G. Wiker, H. Emerich, *Phase Transitions* **2011**, *84*, 726.

[52] B. Ravel, M. Newville, *J. Synchrotron Radiat.* **2005**, *12*, 537.

[53] G. Zichittella, Y. Polyhach, R. Tschaggelar, G. Jeschke, J. Pérez-Ramírez, *Angew. Chem., Int. Ed.* **2021**, *60*, 3596.

[54] T. P. Araújo, A. Shah, C. Mondelli, J. A. Stewart, D. Curulla Ferré, J. Pérez-Ramírez, *Appl. Catal., B* **2021**, *285*, 119878.

[55] G. Kresse, J. Furthmüller, *Comput. Mater. Sci.* **1996**, *6*, 15.

[56] G. Kresse, J. Furthmüller, *Phys. Rev. B* **1996**, *54*, 11169.

[57] J. P. Perdew, K. Burke, M. Ernzerhof, *Phys. Rev. Lett.* **1996**, *77*, 3865.

[58] P. E. Blöchl, *Phys. Rev. B* **1994**, *50*, 17953.

[59] H. J. Monkhorst, J. D. Pack, *Phys. Rev. B* **1976**, *13*, 5188.

[60] Y. Kudoh, H. Takeda, H. Arashi, *Phys. Chem. Miner.* **1986**, *13*, 233.

[61] Z. Q. Xue, Y. Q. Guo, *Adv. Mater.* **2014**, *936*, 181.

**ADVANCED
SCIENCE NEWS**

www.advancedsciencenews.com

**ADVANCED
ENERGY
MATERIALS**

www.advenergymat.de

[62] B. Bondars, G. Heidemane, J. Grabis, K. Laschke, H. Boysen, J. Schneider, F. Frey, *J. Mater. Sci.* **1995**, *30*, 1621.

[63] Z. Liang, W. Wang, M. Zhang, F. Wu, J.-F. Chen, C. Xue, H. Zhao, *Phys. B* **2017**, *511*, 10.

[64] G. Makov, M. C. Payne, *Phys. Rev. B* **1995**, *51*, 4014.

[65] G. Henkelman, B. P. Uberuaga, H. Jónsson, *J. Chem. Phys.* **2000**, *113*, 9901.

[66] T. Pinheiro Araújo, J. Morales-Vidal, T. Zou, M. Agrachev, S. Verstraeten, P. O. Willi, R. N. Grass, G. Jeschke, S. Mitchell, N. López, J. Pérez-Ramírez, *Zenodo.* **2022**, https://doi.org/10.5281/zenodo.7359881.

[67] M. Álvarez-Moreno, C. de Graaf, N. López, F. Maseras, J. M. Poblet, C. Bo, *J. Chem. Inf. Model.* **2015**, *55*, 95.

[68] C. Bo, F. Maseras, N. López, *Nat. Catal.* **2018**, *1*, 809.